Supplemental Material for Classifying Topology in Photonic Heterostructures with Gapless Environments

Kahlil Y. Dixon,[1,*] Terry A. Loring,[2] and Alexander Cerjan[1,†]

[1] *Center for Integrated Nanotechnologies, Sandia National Laboratories, Albuquerque, New Mexico 87185, USA*
[2] *Department of Mathematics and Statistics, University of New Mexico, Albuquerque, New Mexico 87131, USA*

SI. The role of the scaling coefficient κ

In the spectral localizer, Eq. (1) of the main text, κ serves two roles: it ensures that the whole matrix has consistent units, and it serves to tune the spectral localizer. This tuning is necessary because the two simple limits of κ are not useful. When $\kappa = 0$, the spectrum of the spectral localizer is always equally partitioned about the imaginary axis as in this limit L is block diagonal, with blocks $(H - \omega I)$ and $-(H - \omega I)^\dagger$. In the opposite limit, when $\kappa \to \infty$, the spectrum of L simply identifies the joint spectrum of X and Y, which commute. This spectrum of L is also always symmetric about the imaginary axis, for similar reasons as before. From this perspective, it is somewhat remarkable that there is any regime of validity where the spectral localizer approach works at all, given that the two easily computable limits do not contain any new information about the system in question.

However, even though these two limits are boring, for choices of κ in between these two limits the spectrum of L can be highly non-trivial, i.e., when the spectral localizer sees information from both the system's Hamiltonian and position operators with relatively equal strength. Moreover, this range of κ where L is useful is relatively broad. In Fig. S1a, we show the local gap $\mu_{(x,y,\omega)}$ over the same range of positions as is shown in Fig. 2e in the main text, except calculated for values of κ that span a factor of 20. As can be seen, while different values of κ yield modestly different values for $\mu_{(x,y,\omega)}$, the variation in the values of the local gap is significantly reduced to being just a factor of 2. Moreover, in Fig. S1b we show values of κ chosen on a logarithmic scale, and we can confirm that the system's topological index is preserved against different choices of κ over a range of at least $\kappa = 0.0005(2\pi c/a^2)$ to $\kappa = 0.077(2\pi c/a^2)$, i.e. a range in excess of two orders of magnitude.

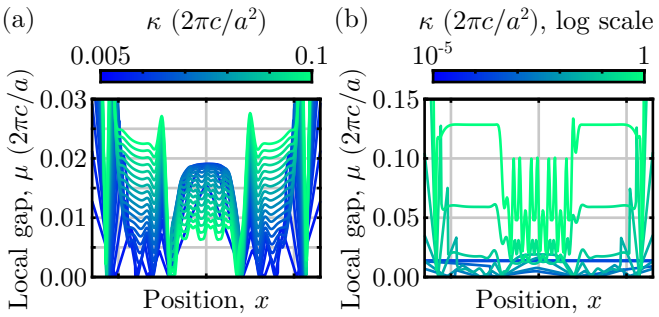

FIG. S1. (a) Local gap $\mu_{(x,y,\omega)}$ calculated for the system from Fig. 2 in the main text along the same positions as is shown in Fig. 2e (i.e., the green line in Fig. 2d). Here, we are using $\omega = 0.37(2\pi c/a)$. The different colored lines are showing linearly spaced values of κ. (b) Similar to (a), except for logarithmicly spaced choices of $\kappa = [1 \cdot 10^{-5}, 3.6 \cdot 10^{-5}, 1.3 \cdot 10^{-4}, 4.6 \cdot 10^{-4}, 0.0017, 0.0060, 0.022, 0.077, 0.28, 1](2\pi c/a^2)$.

But, if small values of the local gap $\mu_{(x,y,\omega)}$ are related to the appearance of localized states in the system, would not the changes in the local gap due to different choices of κ render this theory useless? No. The reason is that bounds on the approximations discussed after Eq. (1) in the main text *also* depend on κ. In particular, the quantities $[H, \kappa X]$ and $[H, \kappa Y]$ feature prominently in predicting the localization of states when $\mu_{(x,y,\omega)} = 0$ [1, Prop. II.4]. Thus, while different values of κ change $\mu_{(x,y,\omega)}$, they also change the bounds in a similar way, yielding a consistent picture.

* kydixon@sandia.gov
† awcerja@sandia.gov

SII. An efficient method for calculating the local index in non-Hermitian systems

Numerically, it is important to approach the determination of the local topological index $C^{\mathrm{L}}_{(x,y,\omega)}$ with some care, especially in photonic systems. For example, the matrices X, Y, H in the system shown in Fig. 2a each have size $\sim 1.2 \cdot 10^6 \times 1.2 \cdot 10^6$ in our discretization. Attempting to calculate all of the eigenvalues of $L_{(x,y,\omega)}(X, Y, H)$ will cause most computers to run out of memory.

In Hermitian systems, one can make use of Sylvester's law of inertia along with a standard $L_{(x,y,\omega)}(X, Y, H) = NDN^\dagger$ decomposition (called the LDLT decomposition) to substantially speed up this process [2, 3]. Here, N is lower-triangular and D is diagonal (and D is *not* equal to a diagonal matrix of the spectrum of $L_{(x,y,\omega)}$). In particular, Sylvester's law states that $\mathrm{sig}(L_{(x,y,\omega)}) = \mathrm{sig}(D)$, and $\mathrm{sig}(D)$ is numerically trivial to calculate given that D is diagonal. Thus, as there are fast methods available to perform LDLT decompositions of sparse matrices, it is relatively easy to find a photonic system's local index.

However, this presents a challenge in non-Hermitian systems where Sylvester's law of inertia no longer applies. Instead, to avoid needing to calculate the full spectrum of $L_{(x,y,\omega)}$, we start by turning off the absorption from the stretched-coordinate perfectly matched layer (PML), yielding a Hermitian system where the LDLT-based method works. In particular, as our PML is implemented as

$$\frac{\partial}{\partial x} \to \frac{1}{1 + \frac{i\sigma_{\max}}{\omega}\left(\frac{x}{L_{\mathrm{PML}}}\right)^3} \frac{\partial}{\partial x} \tag{S1}$$

inside the absorbing boundary region, where $\sigma_{\max}$ is the maximum absorption achieved and L_{PML} is the length of the absorbing layer, the system can be made Hermitian by setting $\sigma_{\max} = 0$ (yielding a system bounded by Dirichlet boundary conditions). A similar formula is used for the PML in y.

Thus, we can determine a non-Hermitian system's local index by starting with a related Hermitian system whose topological markers can be efficiently calculated, slowly turning on the non-Hermiticity, and monitoring the local gap $\mu_{(x,y,\omega)}$ to ensure it remains open. Of course, if $\mu_{(x,y,\omega)} > 0$ along this path of different systems, the index at x, y, ω cannot change as no eigenvalues could have crossed the imaginary axis. For the system we consider in the main text in Fig. 2, we show this evolution of the local gap as a function of the boundary's absorption in Fig. S2. As can be seen, the introduction of the absorption does not yield any new locations within the photonic crystal where $\mu_{(x,y,\omega)} = 0$, meaning that the index of the topological photonic crystal in the center of the system remains the same as its index in a Hermitian version of the system.

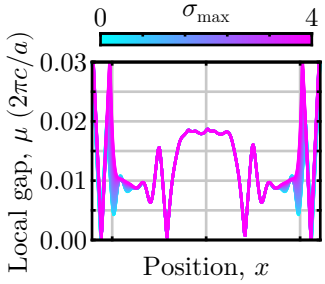

FIG. S2. Local gap $\mu_{(x,y,\omega)}$ calculated for the system from Fig. 2 in the main text along the same positions as is shown in Fig. 2e (i.e., the green line in Fig. 2d). Here, we are using $\omega = 0.37(2\pi c/a)$ and $\kappa = 0.04(2\pi c/a^2)$. The different colored lines are showing linearly spaced values of $\sigma_{\max}$ between 0 and 4, where $\sigma_{\max} = 4$ is the value used in all of the other simulations of the photonic system in this work.

SIII. Additional details on the crystal disorder

In Fig. 3 of the main text, the local gap $\mu_{(x,y,\omega)}$ and local invariant C^{L} are shown for two disorder configurations with different disorder strengths. In Fig. S3, we show the dielectric distribution for these two disorder configurations. These configurations are generated by changing the width, length (major and minor ellipse axes), and position of the dielectric rods (which are circular in the ordered system). In particular, for each rod we generate four uniformly distributed random numbers $\xi_j \in [-0.5, 0.5]$. Two of these random numbers are used to shift the x and y coordinates of the rod's center, $x_{\mathrm{new}} = x_0 + w\xi_1$ and $y_{\mathrm{new}} = y_0 + w\xi_2$, respectively. The other two random numbers treat the

rod as being an ellipse, and change the length of its major and minor axes by $w\xi_j/2$. Here, w parameterizes the geometric strength of the disorder. However, given that the inverse square root of $\bar{\bar{\varepsilon}}$ is what appears in the system's Hamiltonian, see Eq. (4) in the main text, there is no simple relationship between w and $\|\Psi^\dagger \delta H \Psi\|$.

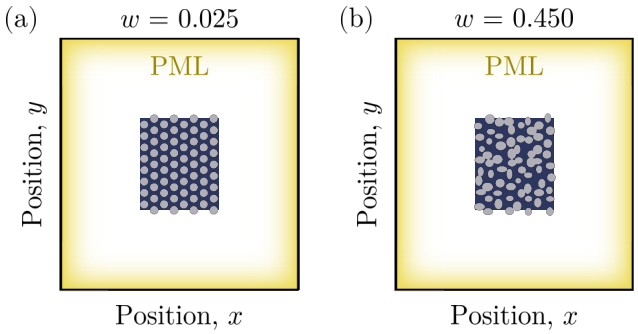

FIG. S3. Schematics showing the geometry of the disordered systems discussed in Fig. 3 of the main text, with geometric disorder strength $w = 0.025$ and $w = 0.45$. These schematics are shown on the same scale as Fig. 2a of the main text.

Additionally, in the calculation of the strength of these disorder configurations, one must make a choice for how many eigenvectors of the ordered system H to retain in Ψ for calculating $\|\Psi^\dagger \delta H \Psi\|$ (this number of retained eigenvectors is m in the relevant discussion surrounding Fig. 3 in the main text, while the total number of possible eigenvectors is n). Of course, $\|\Psi^\dagger \delta H \Psi\|$ must be dependent on m — clearly as $m \to n$, $\|\Psi^\dagger \delta H \Psi\| \to \|\delta H\|$ as the ℓ^2 matrix norm is basis independent. However, for a broad range of choices of $m \geq 180$ that retain only a few hundred eigenvectors of H, we find that $\|\Psi^\dagger \delta H \Psi\|$ is nearly independent of m, see Fig. S4. This justifies our choice of spectral truncation for the disorder strength calculation, and the values quoted in the main text use the largest m shown in Fig. S4, $m = 370$. For this value of m, a disorder parameter of $w = 0.025$ corresponds to a disorder strength of $\|\Psi^\dagger \delta H \Psi\| = 0.026(2\pi c/a)$, and $w = 0.45$ corresponds to $\|\Psi^\dagger \delta H \Psi\| = 0.77(2\pi c/a)$. In the main text, these values are compared against the local gap at the center of the ordered system, $\mu_0 = 0.0185(2\pi c/a)$, which is calculated at $\omega = 0.37(2\pi c/a)$ using $\kappa = 0.04(2\pi c/a^2)$.

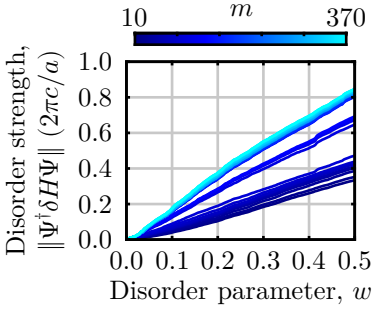

FIG. S4. Dependence of the disorder strength $\|\Psi^\dagger \delta H \Psi\|$ on w, the magnitude of the random numbers chosen to implement the disorder for different choices of m, the number of retained eigenvectors in Ψ. The choices of m are linearly spaced between 10 and 370 in steps of 10.

SIV. Additional plots for increasing free-space dielectric

In Fig. 4a of the main text, we show a series of plots of the local gap as a function of position for increasing free-space dielectric, ε_{fs}. In the main text, these are overlaid to show how the local gap decreases in the system's outer region (with constant ε_{fs}) for increasing outcoupling (i.e., increasing ε_{fs}). However, this makes it difficult to see the appearance of the extra zeros in the local gap at the interface between the two regions. Here, in Fig. S5, we show these same curves separated out so that the formation of these extra locations where $\mu_{(x,y,\omega)} = 0$ can be seen directly.

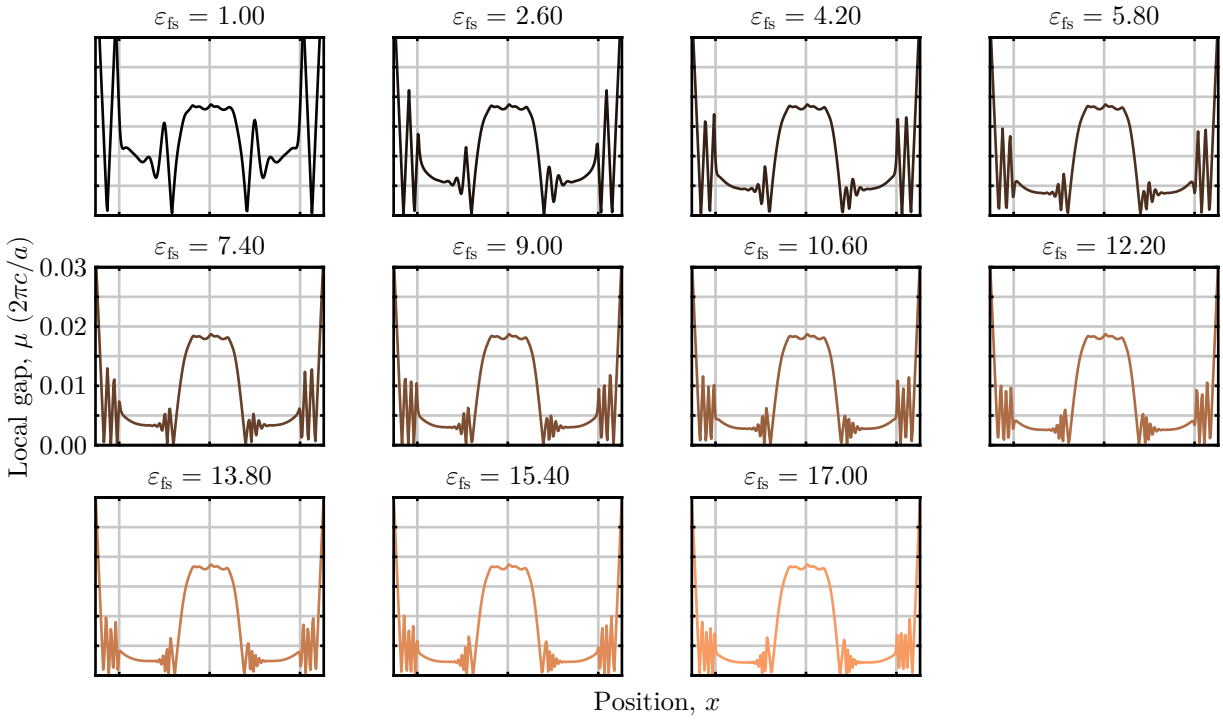

FIG. S5. Local gap for the system shown in Fig. S6a for increasing values of the free space environment's dielectric $\varepsilon_{\rm fs}$. All figures are plotted along the green path in Fig. 2d of the main text, with $\omega = 0.37(2\pi c/a)$ and $\kappa = 0.04(2\pi c/a^2)$.

SV. Classifying the topology of gapless tight-binding heterostructures

While the main text focuses on applications of the spectral localizer to non-Hermitian photonic systems the spectral localizer can be applied to any crystalline system. To demonstrate the broader applications of these methods we consider examples of gapped and gapless topological heterostructures in tight-binding models. Note, unlike the photonic system discussed in the main text, all of tight-binding models we discuss here are Hermitian with open boundary conditions.

To begin, we must first assemble the topological heterostructures. A standard choice of topological insulator is the Chern insulator realized via Haldane's model [4]. The Haldane lattice has the following Hamiltonian:

$$\begin{aligned} H \;=\; & M\sum_{m,n}\left(a^\dagger_{m,n}a_{m,n} - b^\dagger_{m,n}b_{m,n}\right) \\ & - t_1 \sum_{\langle (m,n),(m',n')\rangle} \left(b^\dagger_{m',n'}a_{m,n} + a^\dagger_{m,n}b_{m',n'}\right) \\ & - t_{\rm C} \sum_{\langle\langle (m,n),(m',n')\rangle\rangle} \left(e^{i\phi}a^\dagger_{m',n'}a_{m,n} + e^{-i\phi}a^\dagger_{m,n}a_{m',n'} + e^{i\phi}b^\dagger_{m',n'}b_{m,n} + e^{-i\phi}b^\dagger_{m,n}b_{m',n'}\right). \end{aligned} \tag{S2}$$

This model has two sites per unit cell that form a hexagonal lattice, with annihilation (creation) operators of these sites given in the (m,n)th unit cell by $a_{m,n}$ and $b_{m,n}$ ($a^\dagger_{m,n}$ and $b^\dagger_{m,n}$) with nearest neighbor coupling t_1, onsite energy $M = 0$, and next-nearest neighbor coupling t_C. Here, $\langle\rangle$ denotes a sum over nearest neighbors, while $\langle\langle\rangle\rangle$ denotes the sum is over next-nearest neighbors. To push the Haldane lattice into one of its topological phases, we set $t_1 = t$, $M = 0$, $t_C = t/2$, and $\phi = \pi/2$, see Fig. S6b. For a strip of this material we can calculate the ribbon band structure as seen in Fig. S6b, where the chiral edge states are clearly visible crossing through the system's bulk band gap. However, to form topological heterostructures, we need to create a material to interface with this topological insulator.

To simplify the choice of interface coupling we use a Haldane lattice in its trivial phase as the topologically distinct insulator and a trivialized metallized Haldane lattice for the topologically distinct gapless material. To trivialize either Haldane system we set $t_C = 0$ and set the onsite energy $M = \pm 2\sqrt{3}$ for the trivial insulator and $M = \pm\sqrt{3}/2$ for the trivial metal. To metallize the Haldane system we couple it to a trivial metallic triangular lattice (so that there are

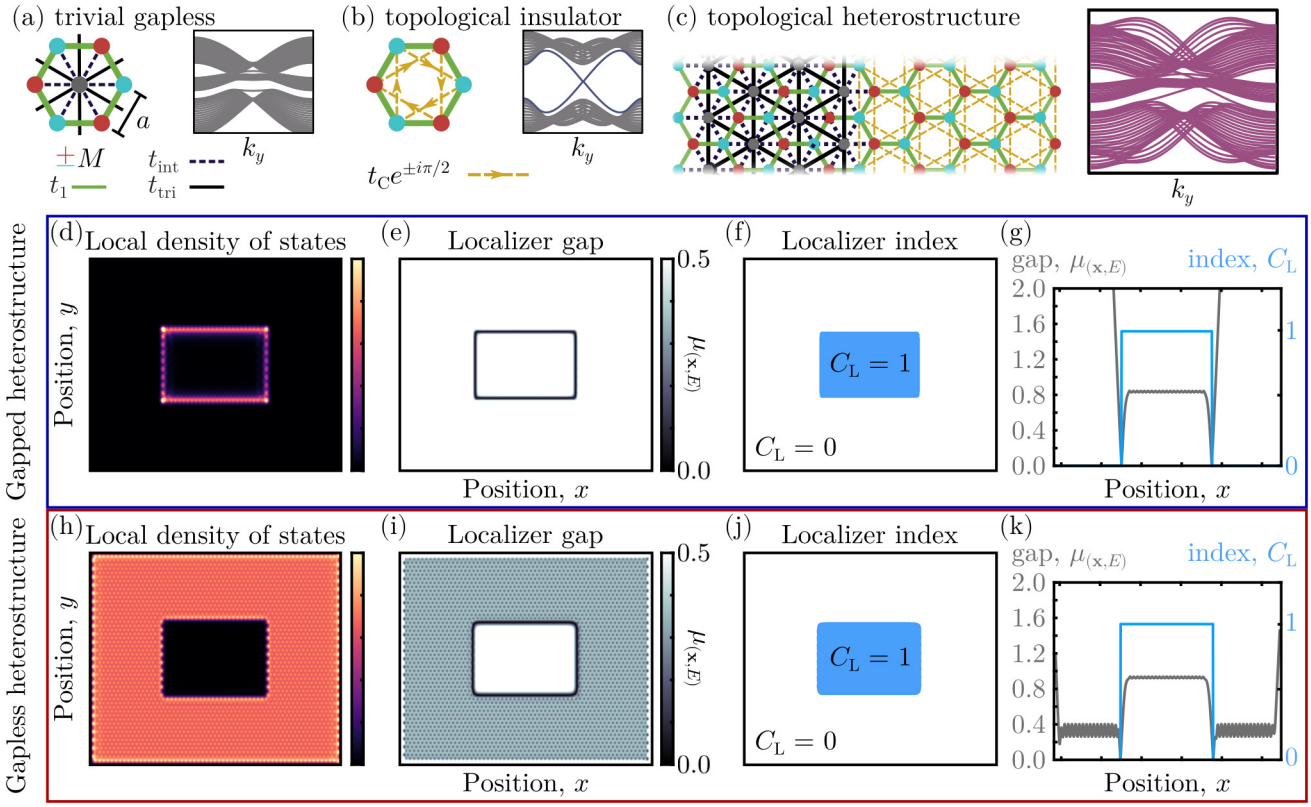

FIG. S6. (a) Schematic and ribbon band structure for a honeycomb lattice (red and blue vertices) with an interstitial triangular lattice (gray vertices), with honeycomb site couplings t_1, triangular site couplings $t_{\rm tri}$, and honeycomb-triangle couplings $t_{\rm int}$. The ribbon band structure is calculated using $t_1 = t$, $t_{\rm C} = 0$, $t_{\rm tri} = 0.2t$, $t_{\rm int} = 0.3t$, $M = \pm\sqrt{3}/2$, and $M_{\rm tri} = 0$. (b) Schematic and ribbon band structure of a Haldane topological insulator with direction-dependent next-nearest neighbor couplings $t_{\rm C}e^{\pm i\pi/2}$. The ribbon band structure is calculated using $t_1 = t$, $M = 0$, $t_{\rm C} = 0.5t$, $\phi = \pi/2$. (c) Schematic and ribbon band structure for a heterostructure formed between the lattices in (a) and (b). (d-f) LDOS (d), localizer gap (e), and local index (f) at $E = 0$ for a heterostructure formed by a trivial insulating Haldane lattice described by Eq. (S2) with $t_1 = t$, $t_{\rm C} = 0$, and $M = \pm 4\sqrt{3}/2$, surrounding a Haldane topological insulating lattice with $t_1 = t$, $M = 0$, $t_{\rm C} = 0.5t$, $\phi = \pi/2$. All three plots are shown on the same spatial scale, with a system surrounded by open boundary conditions. (g) Horizontal line cut of the localizer gap and index through the system's center at $E = 0$. (h-k) Similar to (d-g), except with a gapless outer lattice described by Eq. (S3) with $t_1 = t$, $t_{\rm C} = 0$, $t_{\rm tri} = 0.2t$, $t_{\rm int} = 0.3t$, $M = \pm\sqrt{3}/2$, and $M_{\rm tri} = 0$. For all calculations using the spectral localizer, $\kappa = t/a$ is used.

now 3 sites per unit cell, i.e., the grey, red, and blue sites in Fig. S6), with an inter-lattice coupling strength $t_{\rm int} = 0.3t$ [5, 6]. We set the coupling strength within the triangular lattice to be $t_{\rm tri} = 0.2t$. Altogether, the Hamiltonian for a metallized Haldane lattice is written as

$$\begin{aligned} H \;=\; & M\sum_{m,n}\left(a^\dagger_{m,n}a_{m,n} - b^\dagger_{m,n}b_{m,n}\right) + M_{\rm tri}\sum_{m,n}\left(c^\dagger_{m,n}c_{m,n}\right) \\ & - t_1 \sum_{\langle(m,n),(m',n')\rangle}\left(b^\dagger_{m',n'}a_{m,n} + a^\dagger_{m,n}b_{m',n'}\right) - t_{\rm tri}\sum_{\langle(m,n),(m',n')\rangle}\left(c^\dagger_{m',n'}c_{m,n} + c^\dagger_{m,n}c_{m',n'}\right) \\ & - t_{\rm C}\sum_{\langle\langle(m,n),(m',n')\rangle\rangle}\left(e^{i\phi}a^\dagger_{m',n'}a_{m,n} + e^{-i\phi}a^\dagger_{m,n}a_{m',n'} + e^{i\phi}b^\dagger_{m',n'}b_{m,n} + e^{-i\phi}b^\dagger_{m,n}b_{m',n'}\right) \\ & - t_{\rm int}\sum_{\langle(m,n),(m',n')\rangle}\left(a^\dagger_{m',n'}c_{m,n} + c^\dagger_{m,n}a_{m',n'} + b^\dagger_{m',n'}c_{m,n} + c^\dagger_{m,n}b_{m',n'}\right). \end{aligned} \tag{S3}$$

Here, $c_{m,n}$ ($c^\dagger_{m,n}$) is the annihilation (creation) operator for the triangular lattice site in the (m,n)th unit cell. A strip of the trivial metallic Haldane lattice is used to calculate the ribbon band structure in Fig. S6a.

Concatenating both systems from Fig. S6a and Fig. S6b into a gapless topological heterostructure forms a system

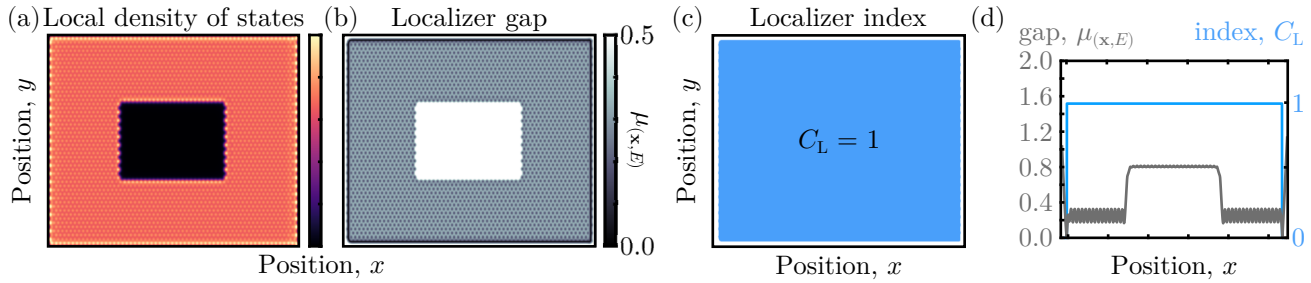

FIG. S7. (a-c) Show the LDOS (a), localizer gap (b), and localizer index (c) at $E = 0$ for a gapless heterostructure formed with an inner Haldane topological insulator (same as Fig. S6), and a gapless topological outer lattice described by Eq. (S3) that incorporates direction-dependent next-nearest neighbor couplings with $t_1 = t$, $t_{\mathrm{tri}} = 0.2t$, $t_{\mathrm{int}} = 0.3t$, $M = 0$, $M_{\mathrm{tri}} = 0$, $t_{\mathrm{C}} = t/2$, and $\phi = \pi/2$. All three plots are shown on the same spatial scale, with open boundary conditions. (d) Horizontal line cut of the localizer gap and index through the system's center and at $E = 0$. For all calculations using the spectral localizer, $\kappa = t/a$ is used.

with a band structure that reproduces the challenge associated with gapless topological heterostructures discussed in the main text, see Fig. S6c. In the band structure calculations, the bands corresponding to interface-localized states are obscured by the degenerate bulk bands from the interstitial triangular lattice. Within this energy range, it is not possible to use topological band theory to identify the existence of interface-localized chiral modes — the heterostructure does not exhibit a common bulk band gap between the two constituent materials so band theory cannot be used to predict a measure of protection, and the edge states cannot be uniquely identified at some energy and wavevector.

The challenges involved in identifying the topology of the gapless heterostructure remain apparent in the system's local density of states (LDOS). In Fig. S6d and h, we show the LDOS within the topological insulator's bulk band gap $E = 0$ for finite gapped and gapless heterostructures, respectively. For both systems, the inner material is a topological insulator, the outer material is topologically trivial, and the outer-most boundary of the outer material has open (Dirichlet) boundary conditions. While the chiral edge states at this energy can be clearly identified in the gapped heterostructure's LDOS, Fig. S6d, the states due to the interstitial triangular lattice's band in Fig. S6h prohibit the numerical observation of any chiral edge states.

We can use the spectral localizer [7–9] to prove that the gapless topological heterostructure in Fig. S6h-k still possesses boundary-localized resonances that are connected to the non-trivial topology of the central lattice. For a 2-dimensional Hermitian tight-binding model, the local marker and protection at position $\mathbf{x}$ and energy E are found by first forming the spectral localizer:

$$L_{(\mathbf{x},E)}(\mathbf{X}, H) = \kappa(X_1 - x_1 I) \otimes \sigma_x + \kappa(X_2 - x_2 I) \otimes \sigma_y + (H - EI) \otimes \sigma_z, \tag{S4}$$

where $\mathbf{X} = (X_1, X_2)^T$, X_j is the j^{th} position operator, $\mathbf{x} = (x_1, x_2)^T$, x_j is the j^{th} position coordinate, σ_j are the Pauli spin matrices, κ is a positive scaling coefficient with units of energy times inverse distance, and I is the identity matrix.

Using the spectral localizer gap and index, we resolved the local Chern numbers for both topological heterostructures shown in Fig. S6, and numerically observe that all substructures are comprised of materials with different invariants in their bulk. Moreover, for the gapless system, applying the spectral localizer and plotting the local gap versus position shows the closing of $\mu_{(\mathbf{x},E)}$ near the heterostructure's interface where the local marker changes, which requires the system to possess topological edge resonances even if they are obscured in the LDOS. Finally, we note that the small, but non-zero, local gap $\mu_{(\mathbf{x},E)}$ on both sides of the heterostructure's interface guarantees the edge resonance's protection against modest system perturbations. As tight binding models are not unbounded operators, they are not subject to the considerations discussed in the main text surrounding the difficulty of defining the strength of a perturbation through its matrix norm. Instead, we are left with the standard topological protection predicted by the spectral localizer: a perturbation δH that is weaker than the local gap, $\|\delta H\| < \mu_{(\mathbf{x},E)}$, cannot change the system's local topology at $(\mathbf{x}, E)$ [7].

To further prove that the interface-localized resonance in a gapless heterostructure can be attributed to the change in the materials' bulk invariants, i.e., that bulk-boundary correspondence still holds for gapless heterostructures, we slightly modify the gapless material on the exterior of the heterostructure to possess the same bulk invariant as the central insulating material, see Fig. S7. This is constructed from the same topological Haldane lattice that is then coupled to the trivial gapless triangular lattice. The result is a gapless topological structure with degenerate bulk and a topological edge state protected by a local gap [10].

Now, we see that the system is no longer a topological heterostructure; the local gap $\mu_{(\mathbf{x},E)}$ no longer closes at the interface between the two materials, indicating the disappearance of the topological interface-localized resonances, while the local maker is seen to be uniform across the entire crystal. Furthermore, the local gap closes around the system's perimeter due to the use of open boundary conditions, indicating a topological phase transition between the outer lattice material and the surrounding (insulating) vacuum.

SVI. Relationship between the Hermitian and non-Hermitian spectral localizers

The spectral localizer for Hermitian systems, Eq. (S4), is similar to its non-Hermitian generalization, Eq. (1) in the main text, except that the conjugate transpose of the lower right-side block $-(H-EI)$ is not taken (or equivalently can be dropped, because $-(H-EI)^\dagger = -(H-EI)$ when the system is Hermitian). Nevertheless, the non-Hermitian spectral localizer in Eq. (1) has been mathematically proven to be the correct generalization of Eq. (S4) to line-gapped non-Hermitian systems such that all of the Chern-related topological properties are correctly counted [11].

Here, we conjecture that Eq. (1) in the main text is the correct non-Hermitian generalization of Eq. (S4) for two physically motivated reasons. First, Eq. (1) reduces to Eq. (S4) when H becomes Hermitian. Second, because this specific change introduces information contained in the non-Hermitian Hamiltonian's left eigenvectors. To see this second reason, note that if $\kappa = 0$, the eigenvectors of $L_{(x,y,\omega)}$ come in two varieties

$$\begin{pmatrix} H-\omega I & 0 \\ 0 & -(H-\omega I)^\dagger \end{pmatrix} \begin{pmatrix} \boldsymbol{\psi}_n \\ 0 \end{pmatrix} = (\omega_n - \omega) \begin{pmatrix} \boldsymbol{\psi}_n \\ 0 \end{pmatrix}$$
$$\begin{pmatrix} H-\omega I & 0 \\ 0 & -(H-\omega I)^\dagger \end{pmatrix} \begin{pmatrix} 0 \\ \boldsymbol{\phi}_m \end{pmatrix} = -(\omega_m^* - \omega) \begin{pmatrix} 0 \\ \boldsymbol{\phi}_m \end{pmatrix}$$

where $H\boldsymbol{\psi}_n = \omega_n \boldsymbol{\psi}_n$ and $H^\dagger \boldsymbol{\phi}_m = \omega_m^* \boldsymbol{\phi}_m$. But, as $(H^\dagger \boldsymbol{\phi}_m)^\dagger = \boldsymbol{\phi}_m^\dagger H = \boldsymbol{\phi}_m^\dagger \omega_m$, $\boldsymbol{\phi}_m^\dagger$ is a left eigenvector of H. While in a Hermitian system, the left and right eigenvectors of H are related by $\boldsymbol{\phi}_m^\dagger = \boldsymbol{\psi}_m^\dagger$, this is not generally true for non-Hermitian systems, $\boldsymbol{\phi}_m^\dagger \neq \boldsymbol{\psi}_m^\dagger$. Moreover, in many non-Hermitian systems, there is relevant information carried in the system's left eigenvectors that is generally not present in the system's right eigenvectors, for example, in parity-time symmetric systems [12] that can exhibit exceptional points. Thus, it seems reasonable that the non-Hermitian spectral localizer (with $\kappa \neq 0$) would need access to this information to correctly determine a system's topological properties, given that quantities like the non-Hermitian Chern number (calculated via band theory) typically make use of both a non-Hermitian system's left and right eigenvectors [13].

[1] A. Cerjan, T. A. Loring, and F. Vides, Quadratic pseudospectrum for identifying localized states, J. Math. Phys. **64**, 023501 (2023).
[2] J. Sylvester, XIX. A demonstration of the theorem that every homogeneous quadratic polynomial is reducible by real orthogonal substitutions to the form of a sum of positive and negative squares, The London, Edinburgh, and Dublin Philosophical Magazine and Journal of Science **4**, 138 (1852).
[3] N. J. Higham, Sylvester's Influence on Applied Mathematics, Mathematics Today **50**, 202 (2014).
[4] F. D. M. Haldane, Model for a Quantum Hall Effect without Landau Levels: Condensed-Matter Realization of the "Parity Anomaly", Phys. Rev. Lett. **61**, 2015 (1988).
[5] D. L. Bergman and G. Refael, Bulk metals with helical surface states, Phys. Rev. B **82**, 195417 (2010).
[6] A. Junck, K. W. Kim, D. L. Bergman, T. Pereg-Barnea, and G. Refael, Transport through a disordered topological-metal strip, Phys. Rev. B **87**, 235114 (2013).
[7] T. A. Loring, K-theory and pseudospectra for topological insulators, Ann. Physics **356**, 383 (2015).
[8] T. A. Loring and H. Schulz-Baldes, Finite volume calculation of k-theory invariants, New York Journal of Mathematics **23**, 1111 (2017).
[9] T. A. Loring and H. Schulz-Baldes, The spectral localizer for even index pairings, Journal of Noncommutative Geometry **14**, 1 (2020).
[10] A. Cerjan and T. A. Loring, Local invariants identify topology in metals and gapless systems, Phys. Rev. B **106**, 064109 (2022).
[11] A. Cerjan, L. Koekenbier, and H. Schulz-Baldes, Spectral localizer for line-gapped non-hermitian systems, Journal of Mathematical Physics **64**, 082102 (2023).
[12] A. Li, H. Wei, M. Cotrufo, W. Chen, S. Mann, X. Ni, B. Xu, J. Chen, J. Wang, S. Fan, C.-W. Qiu, A. Alù, and L. Chen, Exceptional points and non-Hermitian photonics at the nanoscale, Nat. Nanotechnol. **18**, 706 (2023).

[13] H. Shen, B. Zhen, and L. Fu, Topological Band Theory for Non-Hermitian Hamiltonians, Phys. Rev. Lett. **120**, 146402 (2018).